Check for updates

*steel research international*

steel research international

RESEARCH ARTICLE OPEN ACCESS

*Editor's Choice*

# Hybrid Temperature Modeling for the Ruhrstahl–Heraeus Process: Coupling a Data-Driven Approach With a Physics-Based Process Model

Daniel Kavić[1,2] | Michael Bernhard[3] | Hannes Prousch[2] | Roman Rössler[3] | Christian Bernhard[2]

[1]K1-MET GmbH, Linz, Austria | [2]Department Metallurgy, Montanuniversitat Leoben, Leoben, Austria | [3]voestalpine Stahl GmbH, Linz, Austria

**Correspondence:** Daniel Kavić (daniel.kavic@k1-met.com)

**Received:** 12 May 2026 | **Revised:** 31 August 2026 | **Accepted:** 10 September 2026

**Keywords:** computational thermodynamics | hybrid modeling | Ruhrstahl–Heraeus degasser | secondary steelmaking | temperature modeling

## ABSTRACT

The Ruhrstahl–Heraeus (RH) vacuum degassing process is a key technology in modern steelmaking for producing high-performance steel grades, performing degassing, decarburization, inclusion separation and modification, and high-yield alloying in a single unit. Since RH treatment is often the final step before continuous casting, robust process control and reliable temperature monitoring are essential. This work presents a hybrid temperature model for continuous temperature prediction during the RH process. Enthalpy contributions from alloying additions, including the sensible heat required to reach melting temperature ($\Delta H_{heat}$), the enthalpy of fusion ($\Delta H_{fus}$) where applicable, and the integral enthalpy of mixing or dissolution ($\Delta H_{mix}$), as well as reaction enthalpies ($\Delta H_R$), are derived from thermodynamic calculations using FactSage databases. These values represent the exothermic and endothermic heat changes arising from physicochemical interactions among elements within the system. Heat losses by radiation and convection are included, together with an unsteady-state term representing heat-up of the cold vacuum vessel, parameterized by multiple linear regression based on a recent study by the authors. The model shows excellent agreement, with an RMSE of 2.79 °C, an MAE of 2.16 °C, and an $R^2$ of 0.98.

## 1 | Introduction

The Ruhrstahl–Heraeus (RH) vacuum degassing unit is an indispensable component of modern steelmaking, particularly for plants targeting the production of high-performance steel grades. Owing to its broad process capabilities, including removal of dissolved H and N, decarburization, extensive separation of nonmetallic inclusions, inclusion modification by CaSi wire injection, and the addition of large amounts of alloying additions with high yield, RH treatment plays a key role in meeting demanding requirements regarding cleanliness and composition. In many production routes, RH processing also represents the final step of secondary steelmaking before continuous casting, which further raises the importance of reliable temperature control and accurate endpoint prediction.

Precise control of the casting temperature is critical for both product quality and process stability [1]. Excessive superheating can promote pronounced center segregations and increase the risk of strand shell breakouts due to reduced solidification rates [2]. Conversely, if the steel temperature is too low, severe submerged entry nozzle (SEN) clogging may occur during casting, leading to considerable contamination of the product. In the worst case, undercooling can even force casting interruptions when the melt falls below liquidus temperature and solidifies in the SEN or tundish.

Since a single RH treatment may consist of multiple metallurgical operations, processing times of an hour or more are common, over which the steel temperature can drop significantly. In contrast, alloying large quantities of Al and Si, e.g., during the production

This is an open access article under the terms of the Creative Commons Attribution License, which permits use, distribution and reproduction in any medium, provided the original work is properly cited.

© 2026 The Author(s). *steel research international* published by Wiley-VCH GmbH.

of electrical steels, provides substantial amounts of energy to the system [3]. To meet the narrow temperature range required at the caster, an appropriate starting temperature needs to be selected, accounting for both negative and positive contributions to the system's heat balance throughout the RH process.

Given this strong sensitivity of downstream process stability and product quality to temperature deviations, extensive temperature models have been developed for secondary metallurgical treatments, most prominently for the ladle furnace [4–11]. However, RH vacuum refining has received increasing attention in recent years [12–17]. The majority of published RH endpoint–temperature models are data-driven "black box" approaches, which require large and sufficiently diverse process datasets to capture all relevant phenomena.

For example, Feng et al. [12] proposed a case-based reasoning (CBR) model for predicting the final steel temperature after RH treatment using a production dataset of 2500 heats. The workflow combined multiple linear regression (MLR) with an analytic hierarchy process to derive the attribute weights. In a subsequent study, the same authors refined the CBR framework by optimizing attribute weights *via* a genetic algorithm, reporting 78.3% of predictions within ±5 °C error range and outperforming conventional CBR, back-propagation neural networks (BPNN), and MLR [13]. Bao et al. [14] employed a cloud model [18, 19], which was trained on 300 heats. It was reported that 73.7% of predictions were within ±5 °C margin, exceeding the accuracy of a BPNN reference model.

Gu et al. [15] combined principal component analysis (PCA) with CBR and achieved 69.7% within ±5 °C. Yang et al. [16] presented an endpoint-temperature model integrating an artificial neural network with multiprocess operation simulation, reporting hit ratios above 90% within ±5 °C. Similarly, Baotang et al. [17] combined PCA, BPNN, and particle swarm optimization using 711 RH samples, reaching up to 92.2% within ±5 °C error band.

A key limitation of purely data-driven models is their inability to predict continuous temperature profiles, providing only endpoint temperature estimates and offering limited robustness outside the training domain. When process conditions deviate from those represented in the training data (edge-case regimes), the model may deliver unreliable extrapolations and large prediction errors. Mechanistic ("white box") formulations are therefore frequently used as a complement, particularly when robust behavior outside the training-data regime is required.

Consequently, hybrid ("grey box") approaches have emerged, using physical principles to constrain or quantify boundary conditions that cannot be reliably estimated with data-driven methods alone.

Accordingly, the present work employs a modeling framework based on the hybrid temperature modeling concept previously established for the ladle furnace (LF) [11]. The model covers heat losses to the environment due to radiation and convection and to the cold vacuum vessel due to convection, which are parameterized using MLR coefficients obtained in prior work [3]. In addition, the established RH reaction kinetics model developed by Kavić et al. [20] is adopted as the kinetic basis of the present study. This RH model accounts for all relevant chemical reactions and alloying additions. However, since enthalpy changes during treatment were not considered, the original version was formulated as an isothermal model.

To incorporate enthalpy effects into the hybrid RH model, the relevant thermochemical contributions are precomputed and stored in lookup and reaction tables. These contributions include the enthalpy changes associated with alloying, namely, the sensible heat required to reach melting temperature ($\Delta H_{\mathrm{heat}}$), the enthalpy of fusion ($\Delta H_{\mathrm{fus}}$), the integral enthalpy of mixing or dissolution calculated as the sum of partial mixing contributions $\left(\Delta H_{\mathrm{mix}}(T,P,n) = \sum_i n_i \left(\frac{\partial \Delta H_{\mathrm{mix}}}{\partial n_i}\right)_{T,p,n_{i\neq j}}\right)$, and reaction enthalpies ($\Delta H_{\mathrm{R}}$). This strategy differs from the LF temperature model [11], where the ChemApp [21] application interface was used to directly access FactSage [22] thermodynamic databases during runtime.

Finally, the resulting hybrid temperature model is validated and critically assessed using 13 industrial heats with a total of 90 temperature measurements.

## 2 | Hybrid Temperature Modeling Framework

### 2.1 | Associated Heat Balance and Flows During RH Operation

Metallurgical operations during RH treatment may involve decarburization, degassing, removal of nonmetallic inclusions for improved steel cleanliness, and the addition of alloying and deoxidizing agents, often in the order of several tonnes per heat. Since each operation has a different effect on the system's heat balance and an RH treatment potentially consisting of multiple operations at once, precise temperature control represents a key challenge. The melt's starting temperature, which is typically set during the final stage of basic oxygen furnace (BOF) or LF operation [11], must account for heat losses during RH treatment and the subsequent casting process, as well as for heat provided by alloying. Therefore, a comprehensive understanding of heat losses and heat inputs during the RH process is fundamental. The overall heat balance can be divided into the following main contributions, as can be seen in Figure 1.

1. Thermal state of the vacuum vessel, $\dot{Q}_{\mathrm{vessel}}$: The thermal condition of the vacuum vessel has a major impact on the temperature decrease during the first period of the treatment. Until thermal equilibrium is reached, quantifying this parameter is only possible to a limited extent because it depends on numerous factors, e.g., preheating of the vessel lining, repair work on the snorkels, the turnover time between two consecutive treatments, the treatment duration of the preceding heat, etc.
2. Heat losses to the surroundings, $\dot{Q}_{\mathrm{surrounding}}$: In addition to the temperature losses arising from the unsteady thermal state of the vessel, radiative and convective heat losses from the ladle's outer wall, the slag surface, and the vacuum vessel to the environment must be considered.



1869344x, 0, Downloaded from https://onlinelibrary.wiley.com/doi/10.1002/srin.70722 by Daniel Kavi - CochraneAustria , Wiley Online Library on [14/10/2026]. See the Terms and Conditions (https://onlinelibrary.wiley.com/terms-and-conditions) on Wiley Online Library for rules of use; OA articles are governed by the applicable Creative Commons License

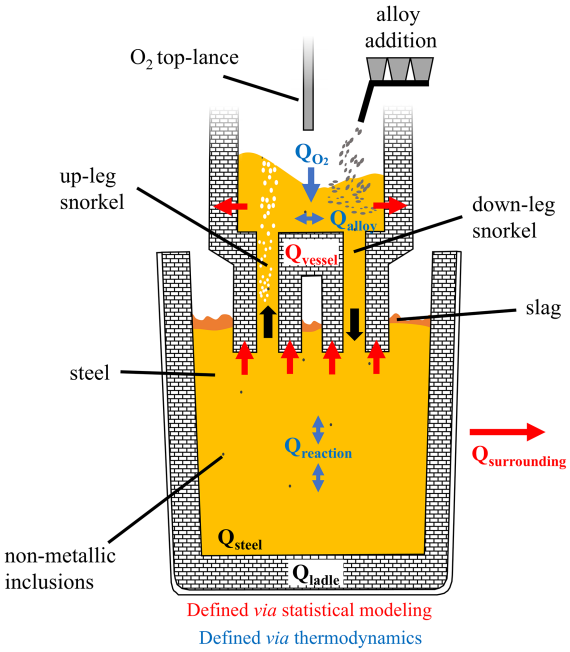


**FIGURE 1** | Schematic representation of the Ruhrstahl–Heraeus vacuum degassing unit, including $O_2$ top-lance blowing, alloying, steel circulation through the up-leg and down-leg snorkels, and the main heat-transfer phenomena considered during refining.

3. Heat effects of chemical reactions, $\dot{Q}_R$: A third major contribution arises from chemical reactions occurring in the system, primarily deoxidation, decarburization, and degassing of the steel.
4. Alloying additions, $\dot{Q}_{alloy}$: The addition of alloying elements can cause either a significant decrease or increase in temperature, depending on whether an alloying addition exhibits exothermic or endothermic mixing enthalpies.
5. Oxygen blowing *via* top lance, $\dot{Q}_{O_2}$: $O_2$ blowing through a top lance provides additional energy to the system. This can, in principle, be assigned to contributions (iii) and (iv) but is treated separately due to the process schedule. The reason for the substantial energy release is the oxidation of iron and the subsequent reduction of FeO *via* Al, Si, Mn, and C; the resulting thermal effect includes both reaction and mixing enthalpies.
6. Thermal state of the ladle, $\dot{Q}_{ladle}$: Temperature losses associated with the thermal state of the ladle depend primarily on the turnover time. With increasing turnover time, the lining temperature progressively decreases, resulting in higher heat loss. The temperature drop due to the unsteady thermal state of the ladle is particularly strong during the first few minutes after BOF tapping. However, since LF treatment is typically carried out prior to RH treatment, the unsteady state of the ladle lining is considered to be negligible.

Applying the conservation of energy to the liquid steel bath, the change in the steel enthalpy is determined by the sum of the heat transferred from the steel to the surroundings, as well as the thermal effects of reactions, alloying additions, and oxygen blowing. A consistent sign convention is used throughout this study: Heat transferred to the liquid steel bath is positive, whereas heat withdrawn from the bath is negative. The transient heat balance can therefore be expressed as follows:

$$\frac{dH_{steel}}{dt} = \dot{Q}_{vessel} + \dot{Q}_{surrounding} + \dot{Q}_R + \dot{Q}_{alloy} + \dot{Q}_{O_2} + \dot{Q}_{ladle} \quad (1)$$

where $H_{steel}$ is the total enthalpy of the liquid steel bath in J, and $\dot{Q}_i$ denotes the corresponding heat transfer or heat generation rate in J $s^{-1}$. Consequently, heat losses to the vacuum vessel, ladle lining, and surroundings have negative values, whereas heat inputs have positive values. The reaction and alloying terms may be either positive or negative, depending on whether the respective process is exothermic or endothermic. Integration of Equation (1) over the simulation time step $t_{step}$ gives

$$\Delta H_{steel} = \int_{t_n}^{t_n + t_{step}} (\dot{Q}_{vessel} + \dot{Q}_{surrounding} + \dot{Q}_R + \dot{Q}_{alloy} + \dot{Q}_{O_2} + \dot{Q}_{ladle}) dt \quad (2)$$

Finally, the enthalpy change calculated for each step is converted into a temperature change $\Delta T_{steel}$ in K using the current steel mass $m_{steel}$ in kg and the corresponding heat capacity $c_{p,steel}(T_{steel})$ in J $kg^{-1}$ $K^{-1}$.

$$\Delta T_{steel} = \frac{\Delta H_{steel}}{m_{steel} \cdot c_{p,steel}(T_{steel})} \quad (3)$$

## 2.2 | Concept and Methodology for Hybrid Modeling of RH Operations

In the present work, a hybrid modeling framework was applied to predict the steel bath temperature during RH vacuum degassing. The overall architecture of the model developed is visualized in Figure 2. The present model makes use of thermodynamic calculations performed using FactSage [3, 23–27]. These thermodynamic data were required to quantify the thermal effects of chemical reactions and alloying. However, only enthalpies of reactions expected to occur during the RH process were considered within the model. Furthermore, enthalpy contributions from alloying were extracted for varying addition amounts under different initial temperatures, assuming isothermal conditions. The resulting variation is captured in dedicated lookup tables for each alloying element. A detailed description of the considered chemical reactions and lookup tables is provided in Section 2.3.

During runtime, the thermodynamic data are accessed through a dedicated application interface and coupled to a kinetic tank-in-series approach. The kinetic formulation, which has been described extensively in a previous work [20], provides the reaction progress and mass transfer rates to evaluate chemical heat effects and the transient evolution of the bath composition. Within each time step, the kinetic module retrieves the required thermodynamic quantities from the lookup tables, thereby enabling consistent coupling between reaction progress and thermal effects.

In addition to thermodynamic data, the hybrid model imports the required process data, including the initial steel and slag compositions, the initial steel temperature, deep-vacuum holding times, oxygen-blowing sequences, and alloying addition schedules.



1869344x, 0, Downloaded from https://onlinelibrary.wiley.com/doi/10.1002/srin.70722 by Daniel Kavi - CochraneAustria , Wiley Online Library on [14/10/2026]. See the Terms and Conditions (https://onlinelibrary.wiley.com/terms-and-conditions) on Wiley Online Library for rules of use; OA articles are governed by the applicable Creative Commons License

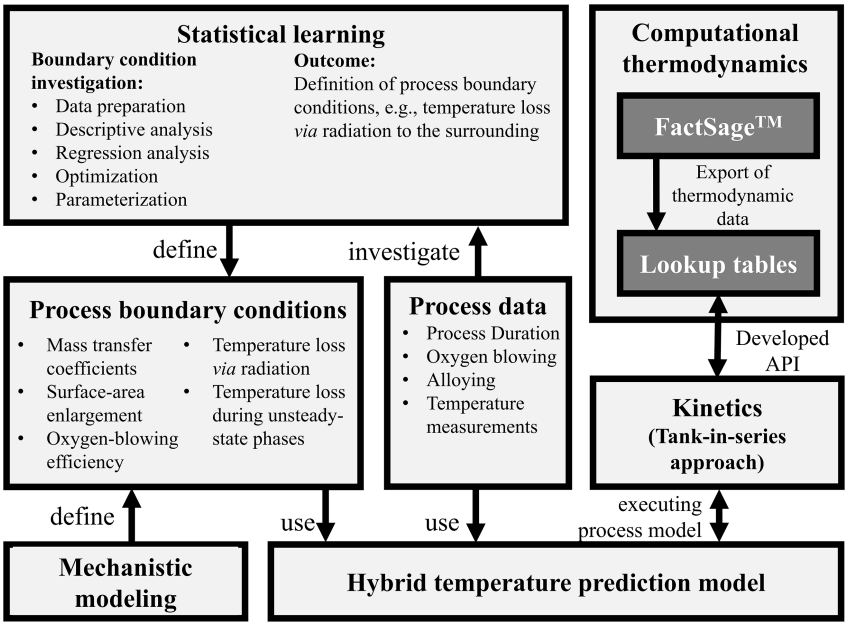


**FIGURE 2** | Conceptual framework of the hybrid temperature prediction model.

Furthermore, the simulation requires a set of process-specific conditions, such as the effective oxygen-absorption rate, mass transfer coefficients, effective surface-area enlargement, and heat loss terms, e.g., radiative losses to the surroundings and the early elevated losses during unsteady-state phases. Depending on the specific boundary condition, parameter values were either adopted from literature or determined by data-driven methods [20, 28].

As indicated in Figure 2, statistical learning was used to investigate and parameterize boundary conditions that cannot be measured directly. In particular, radiative heat losses to the surrounding area were quantified using MLR approaches, as reported in previous work by Bernhard et al. [3]. Consequently, the hybrid framework leverages the tank-in-series approach for kinetic consistency, thermodynamics for released or consumed enthalpies, and statistical learning for a robust estimation of uncertain boundary conditions, resulting in a comprehensive temperature prediction model for RH degassing.

## 2.3 | Considered Chemical Reactions and Thermodynamic Lookup Tables

The thermodynamic data required for deoxidation reactions and the evaluation of decarburization and degassing reactions were extracted from the current FactSage Version 8.4 and the associated referenced literature [29–35].

The reaction set implemented in the model and the corresponding reaction enthalpies $\Delta H_R$ are listed in Table 1. All oxidation reactions represent a major exothermic contribution to the energy balance and can therefore increase the bath temperature depending on the reaction extent. Enthalpy is also released once FeO is reduced by Al, Si, or Mn. A reduction of the slag *via* C would lead to an energy withdrawal from the surroundings and therefore a reduction of the liquid-steel temperature. The thermal effects

**TABLE 1** | Reactions considered in the thermodynamic module and their corresponding reaction enthalpies.

| Reaction | $\Delta H_R$, kJ mol$^{-1}$ | References |
|---|---|---|
| **Oxidation reactions** | | |
| $Al + \frac{3}{4}O_2 \rightarrow \frac{1}{2}Al_2O_3$ | −837.9 | [29, 30] |
| $Si + O_2 \rightarrow SiO_2$ | −910.9 | [30, 31] |
| $Mn + \frac{1}{2}O_2 \rightarrow MnO$ | −385.2 | [29, 30] |
| $C + \frac{1}{2}O_2 \rightarrow CO$ | −110.5 | [32] |
| $Fe + \frac{1}{2}O_2 \rightarrow FeO$ | −234.6 | [33] |
| **FeO reduction reactions** | | |
| $Al + \frac{3}{2}FeO \rightarrow \frac{1}{2}Al_2O_3 + \frac{3}{2}Fe$ | −429.8 | — |
| $Si + 2FeO \rightarrow SiO_2 + 2Fe$ | −366.8 | — |
| $Mn + FeO \rightarrow MnO + Fe$ | −113.2 | — |
| $C + FeO \rightarrow CO + Fe$ | 161.5 | — |
| **Degassing reactions** | | |
| $H \rightarrow \frac{1}{2}H_2$ | −36.4 | [34, 35] |
| $N \rightarrow \frac{1}{2}N_2$ | −3.6 | [35] |

associated with the H and N degassing reactions are small in comparison with the dominant thermal contributions. However, they are included in the model for completeness. The listed $\Delta H$ values were used to quantify $Q_R$ within the coupled kinetic simulation framework.

In addition to the reaction enthalpies, the thermal effect associated with alloying additions was quantified by extracting the sensible heat required to reach melting temperature ($\Delta H_{heat}$), the enthalpy of fusion of solid additions ($\Delta H_{fus}$), and the integral enthalpy of mixing or dissolution calculated as the sum of partial mixing contributions ($\Delta H_{mix}(T, P, n)$) for all alloying



1869344x, 0, Downloaded from https://onlinelibrary.wiley.com/doi/10.1002/srin.70722 by Daniel Kavi - CochraneAustria , Wiley Online Library on [14/10/2026]. See the Terms and Conditions (https://onlinelibrary.wiley.com/terms-and-conditions) on Wiley Online Library for rules of use; OA articles are governed by the applicable Creative Commons License

agents considered in the model. These data constitute the second thermodynamic data set required for evaluating the energy term $Q_{alloy}$.

The enthalpy contributions were generated in the form of two-dimensional lookup tables (temperature- and composition-dependent). Pure liquid iron was used as reference system, and the concentration of the respective alloying element was increased stepwise from 0.00 to 4.00 wt.% in increments of 0.01 wt.%. For each increment, the system's enthalpy change at a specified constant temperature was calculated using FactSage. The enthalpy changes, representing the energy released or absorbed during dissolution and mixing at the predefined temperature, were stored in the lookup tables in J $kg^{-1}$ of steel. The calculations were repeated from 1540 to 1640 °C with a temperature increment of 10 °C. During the transient RH process simulation, the enthalpy change corresponding to the current liquid–steel temperature and alloying-element content was determined by bilinear interpolation between the four nearest temperature-composition data points. Interpolation was restricted to the predefined temperature and composition ranges, and no extrapolation beyond these limits was permitted. The main constituents of the Al, FeSi, and FeMn additions are given in Table 2.

For convenience, the released and consumed enthalpies during these alloying steps have been converted into a $\Delta T$ value using the heat capacity of pure iron. The validity of this approximation was assessed by comparing the resulting $\Delta T$ values with adiabatic equilibrium calculations performed in FactSage over the investigated temperature range of 1540 to 1640 °C and alloy concentrations of up to 4 wt.%. The maximum absolute deviations were 0.42 °C for FeSi, 0.28 °C for Al granules, and 0.18 °C for FeMn. Relative to the corresponding maximum predicted temperature changes, these deviations amount to 1.12%, 1.75%, and 0.21%, respectively. Thus, the use of the heat capacity of pure liquid iron introduces a relative deviation of less than 2% within the investigated parameter range and is considered sufficiently accurate for the present analysis. The resulting temperature differences due to alloying are illustrated in the following Figure 3a–c. Additionally, iso-$\Delta T$ lines were added to the diagrams for better interpretability.

**TABLE 2** | Composition of the alloying material.

| Alloying agent | C, wt.% | Mn, wt.% | Si, wt.% | Al, wt.% | Fe, wt.% |
|---|---|---|---|---|---|
| FeSi | 0.02 | 0 | 74.5 | 0 | Balance |
| Al granules | 0 | 0 | 0.7 | 96 | Balance |
| FeMn | 0.08 | 95 | 0.9 | 0 | Balance |

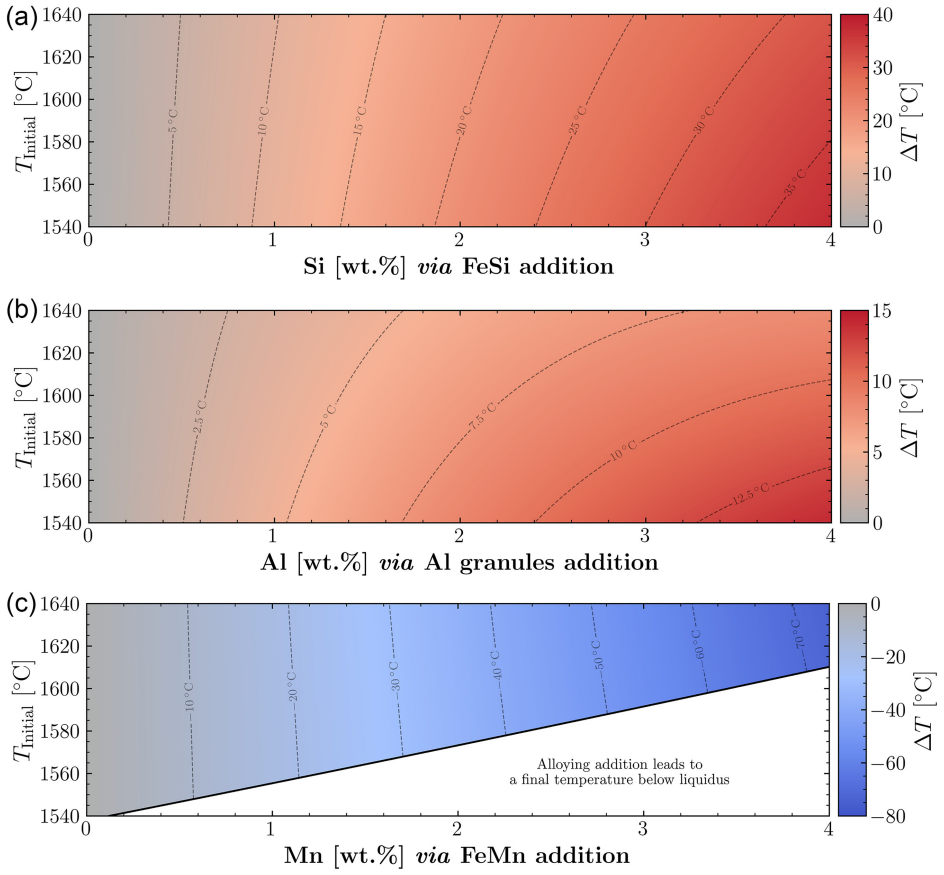


**FIGURE 3** | Calculated temperature change $\Delta T$ as a function of initial steel temperature and alloying-element content for additions of (a) Si *via* FeSi, (b) Al *via* Al granules, and (c) Mn *via* FeMn.



1869344x, 0, Downloaded from https://onlinelibrary.wiley.com/doi/10.1002/srin.70722 by Daniel Kavi - CochraneAustria , Wiley Online Library on [14/10/2026]. See the Terms and Conditions (https://onlinelibrary.wiley.com/terms-and-conditions) on Wiley Online Library for rules of use; OA articles are governed by the applicable Creative Commons License

The addition of FeSi results in the largest temperature increase, attributable to the strongly negative partial mixing enthalpy of Si ($\Delta H_{Si}$). For instance, increasing the Si content of an initially pure iron melt at 1540 °C by 4% heats the bath by 37.5 °C (see Figure 3a). Under identical initial conditions, a 4% increase in Al content only heats the bath by 16 °C (see Figure 3b).

In contrast, most alloying additions absorb heat upon charging and therefore decrease the melt temperature. For low initial melt temperatures and large FeMn additions, the calculated final bulk temperature may fall below the liquidus temperature. Since the current numerical model does not yet account for solid-fraction formation, conditions resulting in a final temperature below liquidus were excluded from the analysis and are outside the scope of the present study. These excluded conditions are indicated by the white triangular region in Figure 3c. It should be noted that the presence of a solid fraction during RH degassing is generally uncommon under industrial operating conditions, particularly for steel grades with higher Mn contents, because sufficient superheat is typically maintained to keep the bulk melt fully liquid. The excluded conditions should therefore be interpreted as limiting cases rather than representative RH operating conditions.

### 2.4 | Statistical Learning Methods Applied

In a prior work [3], the net temperature loss during RH treatment, primarily associated with heat transfer *via* radiation to the surroundings and *via* conduction to the initially cold RH vessel, was quantified from industrial process data (on the order of several thousand heats). Sequential plant temperature measurements were evaluated by defining a temperature drop relative to the last measurement, $\Delta T = T_{start} - T_{finish}$, and relating $\Delta T$ to process variables using MLR. To isolate the initial cooling behavior, cases with negligible exothermic or endothermic heating from alloying additions were considered. The analysis yielded a two-stage cooling characteristic: a strong initial temperature decrease of approximately 1.11 °C $min^{-1}$ during the first treatment stage, attributed to the unsteady thermal conditions of snorkels and refractory surfaces, followed by a lower, quasisteady cooling rate of approximately 0.69 °C $min^{-1}$ for a longer treatment duration as the system approaches thermal equilibrium.

As explicit information on the vessel's thermal state cannot be derived from the available process data, the hybrid model includes one adjustable parameter, namely, the duration of the initial transient period. This parameter accounts for heat-to-heat variations in the initial thermal condition of the RH vessel, which depend on operational factors such as vessel turnover time, the duration of the preceding treatment, lining preheating, and maintenance or repair activities. This parameter exclusively controls the duration of the initial enhanced cooling behavior and does not modify the thermodynamically calculated heat contributions from reactions, alloying additions, or $O_2$ blowing. Future work will focus on dedicated measurements of the refractory temperature and its evolution during subsequent RH treatments.

## 3 | Industrial Process Overview and Provided Data

With more than 3000 steel grades produced *via* both killed and unkilled secondary steelmaking routes, voestalpine Stahl GmbH (VASL) in Linz (Austria) includes a broad spectrum of treatment sequences that need to be represented in process models. Figure 4 provides a schematic overview of the principal approaches typically employed for killed and unkilled steels at VASL, with particular emphasis on RH vacuum refining.

During tapping, primary deoxidation is performed by adding C and Al to the ladle. Depending on the steel grade, deoxidation may be completed at this stage, resulting in fully killed steels. Simultaneously, synthetic slag formers may be added to establish suitable slag conditions for subsequent refining steps at the LF. After both tapping and material additions are concluded, a steel sample is taken, and the bath temperature is measured. Upon arrival at the LF, grade-specific treatments are carried out, including electrical heating, Ar bottom stirring, desulfurization through slag practice, and alloying additions. These operations are designed to set the target temperature for subsequent RH processing and casting while meeting highest cleanness and composition requirements. During LF treatment, melt temperature and composition are measured repeatedly.

At the RH degasser, the applied strategy depends strongly on the steel grade. Killed steels typically undergo relatively short vacuum degassing, followed by final alloying (e.g., microalloying). More complex, though less frequently applied, RH practices for killed steel grades may include an intermediate $O_2$ blowing step to initiate decarburization. In such cases, the steel is subsequently rekilled (typically by Al addition) once decarburization is complete. For unkilled steels, the RH treatment generally starts with decarburization, followed by Al deoxidation. Depending on the grade (e.g., electrical steels), final alloying may involve very large amounts (up to 10 t), resulting in extended treatment times after final deoxidation. Throughout the RH process, the number of temperature measurements and samples taken generally increases with the complexity of the applied refining practice.

Validation of the developed hybrid temperature model was performed using 13 heats provided by VASL, representing a broad range of RH degassing practices. These heats were fully independent of the data used for parameter fitting. The dataset comprises both killed and unkilled steel grades and covers the full range of metallurgical operations occurring during RH degassing treatment (e.g., vacuum degassing, decarburization, oxygen blowing, deoxidation, and alloying). Consequently, a comprehensive and broad spectrum of process influences is represented. For both killed and unkilled heats, the initial steel composition is required. The ranges of the most relevant elements are summarized in Table 3.

Slag composition is of particular importance for unkilled steels, exhibiting elevated FeO and MnO contents. Therefore, a slag sample was taken prior to treatment for all unkilled heats. For the group of killed heats investigated, a single slag sample was collected from one heat as a reference. This approach was adopted because, within a given steel grade, a comparable steel–slag equilibrium is expected due to consistent slag former additions and similar upstream refining conditions during tapping and LF treatment. The corresponding slag compositions for the most relevant constituents are summarized in Table 4.



1869344x, 0, Downloaded from https://onlinelibrary.wiley.com/doi/10.1002/srin.70722 by Daniel Kavi - CochraneAustria , Wiley Online Library on [14/10/2026]. See the Terms and Conditions (https://onlinelibrary.wiley.com/terms-and-conditions) on Wiley Online Library for rules of use; OA articles are governed by the applicable Creative Commons License

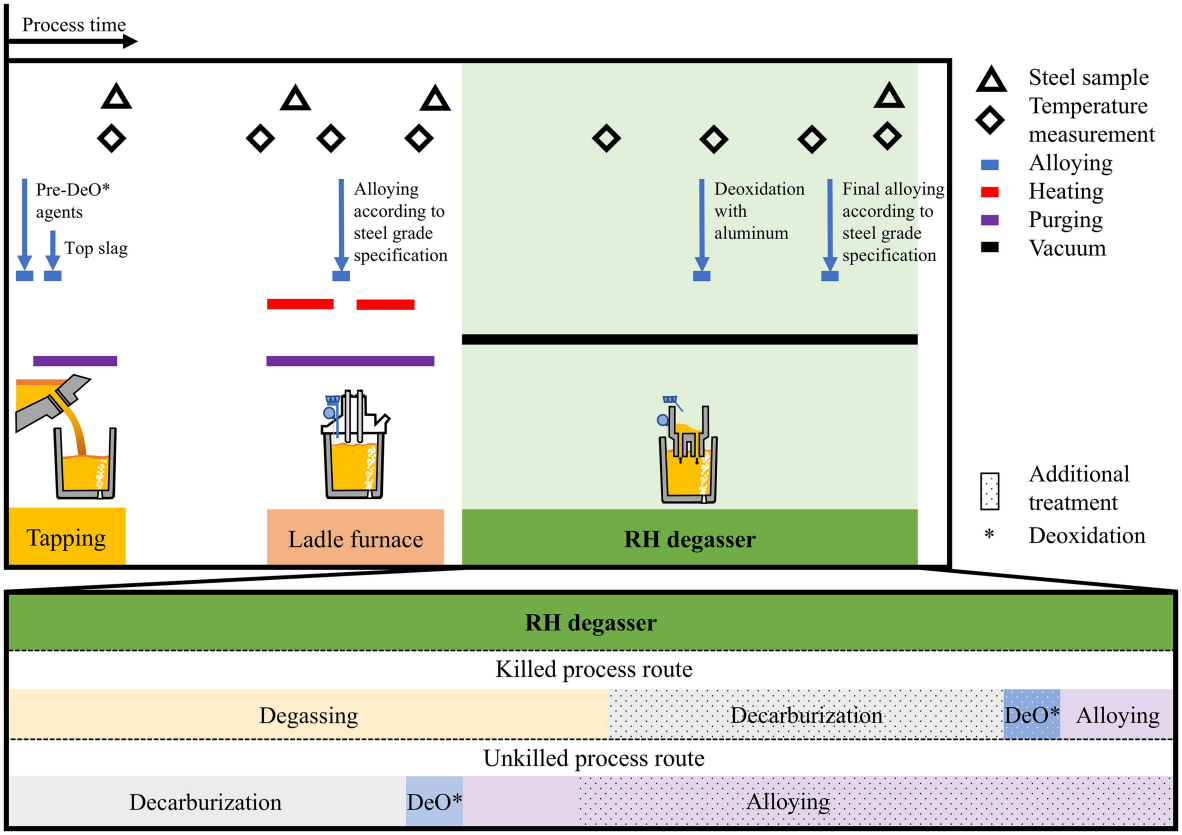


**FIGURE 4** | Secondary steelmaking process routes showing sampling, temperature measurement, alloying, heating, purging, and vacuum treatment steps, together with detailed RH degassing routes for killed and unkilled steel grades.

**TABLE 3** | Initial steel composition ranges of investigated heats.

| Steel grade | C, ppm | O, ppm | Si, ppm | Mn, ppm | Al, ppm |
|---|---|---|---|---|---|
| Killed | 110–280 | 2–8 | 130–460 | 200–690 | 60–530 |
| Unkilled | 250–290 | 363–478 | 10 | 870–1430 | 0 |

Additionally, vacuum pressure profiles, $O_2$ blowing information (including the flow rate and blowing duration), and the initial masses of steel and slag were provided. An overview of the input data is given in Table 5.

Finally, the temperature measurements used for model validation were provided by the industrial partner and acquired at different stages of RH treatment using the plant's standard measurement system. The measurements were performed during regular operation with immersion thermocouple probes from Heraeus Electro-Nite, which are designed for fast and accurate liquid–steel temperature measurements in secondary metallurgy. According to the industrial partner, the measurements exhibit an approximate standard deviation of 1.5 °C and therefore contain an inherent measurement uncertainty.

## 4 | Results and Discussion

### 4.1 | Single Heat Analysis

Two heats, Case IX and Case XI, were selected as representative examples of a killed and an unkilled heat, respectively. Because both heats were sampled at high frequency, they enable a detailed assessment of the hybrid temperature model. Figure 5a,b shows the simulated, continuous temperature development over the full treatment duration. All available temperature measurements are plotted as reference points. To facilitate interpretation, the treatment was divided into specific processes, e.g., degassing, decarburization, and alloying. Furthermore, all alloying additions and $O_2$ blowing intervals are indicated.

**TABLE 4** | Initial slag composition ranges of investigated heats.

| Steel grade | CaO, wt.% | $SiO_2$, wt.% | $Al_2O_3$, wt.% | MgO, wt.% | Fe, wt.% | Mn, wt.% |
|---|---|---|---|---|---|---|
| Killed | 57.6 | 2.4 | 22.7 | 13.7 | 1.9 | 0.4 |
| Unkilled | 42.5–45.8 | 4.9–5.4 | 18.9–21.7 | 9.1–12.4 | 12.4–13.0 | 2.2–2.5 |



1869344x, 0, Downloaded from https://onlinelibrary.wiley.com/doi/10.1002/srin.70722 by Daniel Kavi - CochraneAustria , Wiley Online Library on [14/10/2026]. See the Terms and Conditions (https://onlinelibrary.wiley.com/terms-and-conditions) on Wiley Online Library for rules of use; OA articles are governed by the applicable Creative Commons License

**TABLE 5** | Process parameters for all case studies investigated.

| Case study | Type | Minimum pressure, mbar | Duration until minimum pressure, min | $O_2$ blowing volume, $Nm^3$ | $O_2$ blowing duration, min | Initial steel mass, kg | Initial slag mass, kg |
|---|---|---|---|---|---|---|---|
| I | Killed | 3.3 | 4 | 293 | 19.1 | 167,200 | 3900 |
| II | | 3.7 | 4 | 261 | 15.6 | 173,150 | 2800 |
| III | | 5.1 | 6 | 310 | 20.4 | 167,250 | 3300 |
| IV | | 3.6 | 4 | 207 | 12.1 | 172,000 | 3100 |
| V | | 6.2 | 5 | 190 | 12.6 | 169,900 | 3000 |
| VI | | 3.0 | 4 | 240 | 14.2 | 166,700 | 3000 |
| VII | | 4.9 | 6 | 205 | 14.6 | 163,100 | 3000 |
| VIII | | 2.8 | 6 | 254 | 16.3 | 171,800 | 3100 |
| IX | | 6.2 | 6 | 199 | 12.6 | 164,400 | 3100 |
| X | | 5.6 | 6 | 210 | 14.0 | 168,950 | 3200 |
| XI | Unkilled | 6.0 | 9 | 25 | 2.0 | 172,400 | 3000 |
| XII | | 6.1 | 9 | — | — | 171,237 | 3000 |
| XIII | | 6.3 | 9 | — | — | 173,800 | 3000 |

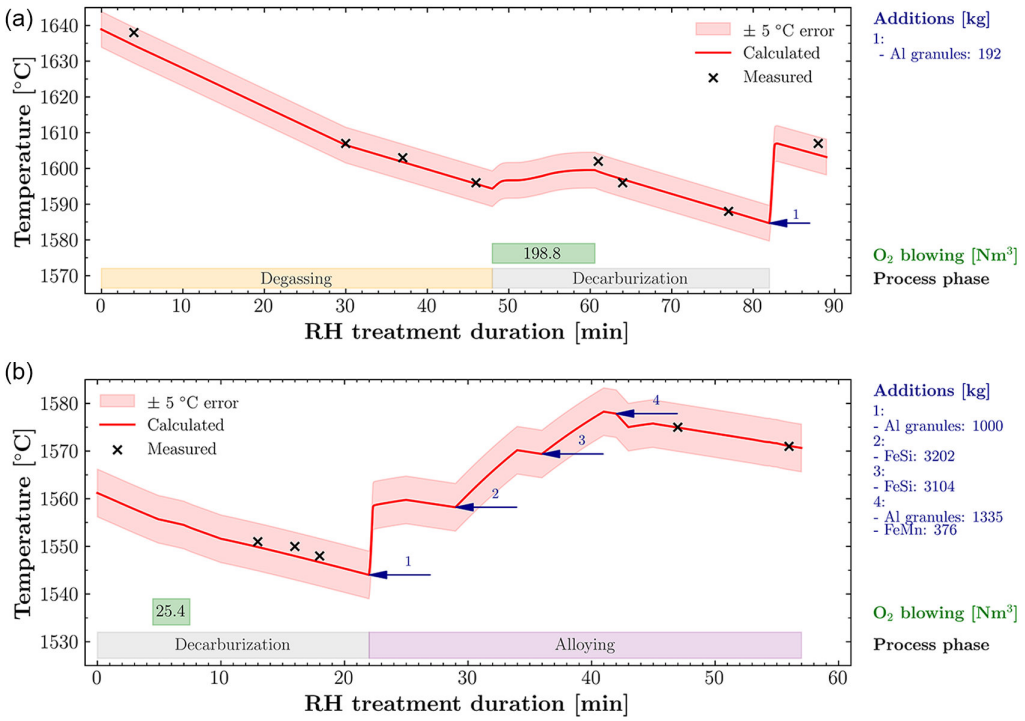


**FIGURE 5** | Calculated and measured temperature profiles during RH treatment for (a) a killed steel grade and (b) an unkilled steel grade.

For Case IX (Figure 5a), an extended initial degassing phase was conducted, during which H and N were removed from the steel by applying a deep vacuum. As the associated enthalpy effects are comparatively small, the melt exhibits a pronounced decrease in temperature driven by ongoing radiative and convective heat losses to the surroundings, as well as by heating of the snorkel until a quasisteady-state thermal condition is reached. Starting from 1638 °C, the temperature decreases by approximately 44 °C within this first phase. With the onset of $O_2$ blowing, the process transitions from degassing to decarburization. The injected $O_2$ promotes substantial slag formation, primarily *via* FeO generation, and subsequently drives the oxidation of Al, Si, Mn, and C. Because of the strong exothermic nature of these oxidation reactions, a net temperature increase is observed in the predictions despite continuous heat losses. Between minutes 48 and 61, the temperature increased by approximately 6 °C. After oxygen blowing, the temperature decreases continuously again until Al granules are charged at minute 82. Al addition results in rapid and effective deoxidation of both the dissolved O in the steel and FeO in the slag. The corresponding exothermic contributions,



1869344x, 0, Downloaded from https://onlinelibrary.wiley.com/doi/10.1002/srin.70722 by Daniel Kavi - CochraneAustria , Wiley Online Library on [14/10/2026]. See the Terms and Conditions (https://onlinelibrary.wiley.com/terms-and-conditions) on Wiley Online Library for rules of use; OA articles are governed by the applicable Creative Commons License

comprising chemical reaction heat as well as solution and mixing effects, result in a temperature increase of approximately 22 °C. Thereafter, the steel temperature diminishes again due to heat losses to the surroundings. The final predicted temperature is 1604 °C, in excellent agreement with the measured value of 1607 °C. Across all measurements, the absolute deviation between simulation and experiment remains below 5 °C.

For Case XI (Figure 5b), the treatment begins with a 22-min decarburization period. During this interval, the temperature decreases from 1561 to 1543 °C. Starting around minute 6, a brief $O_2$ blowing step is performed to introduce additional O into the system, supporting decarburization and providing an additional exothermic contribution to the thermal balance. At minute 22, the addition of 1000 kg Al granules causes a pronounced temperature increase of about 15 °C, consistent with heat release from deoxidation and from solution/mixing enthalpies. At minute 29, ~3.2 t FeSi is charged, resulting again in a temperature increase of 12 °C. During the subsequent FeSi charging (~3.1 t), the temperature gain diminishes to approximately 9 °C, indicating the expected reduction in solution and mixing enthalpy release due to higher initial Si contents in the steel bath (see Figure 3a). In the final charging event, larger amounts of FeMn and Al granules are added. Because of the comparatively high energy demand associated with Mn alloy heating and dissolution, the temperature shows a significant decrease, followed by a rise due to the subsequent Al addition. For the remainder of the treatment, the temperature follows a monotonic decline, reaching a final calculated temperature of 1570 °C, which matches the measured value. Overall, the agreement between measured and computed temperatures is again excellent, with a maximum deviation of approximately 2 °C.

## 4.2 | Analysis of All Investigated Heats

In addition to the detailed analyses, all investigated cases were evaluated with respect to the predictive performance of the hybrid temperature model against the experimentally measured temperatures. The 13 heats were sampled a total of 90 times, providing

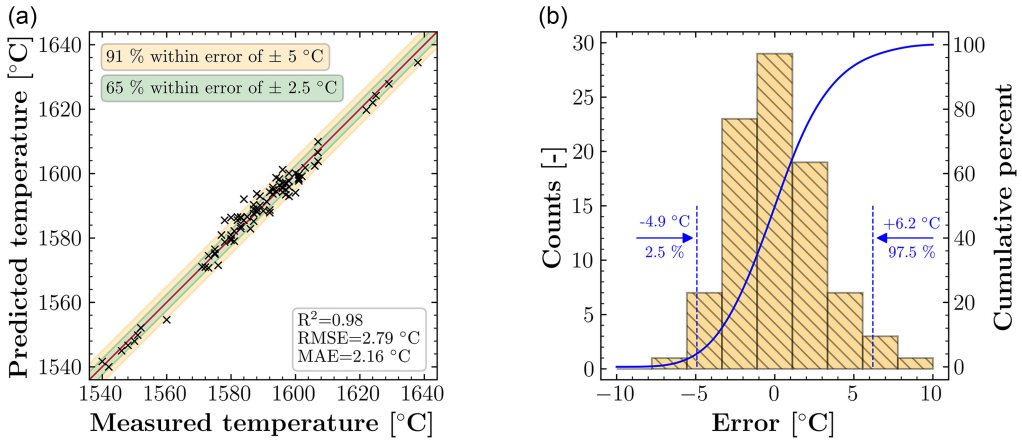


**FIGURE 6** | Evaluation of the continuous temperature prediction model during RH treatment: (a) predicted vs. measured steel temperatures with ±2.5 °C and ±5 °C error bands; (b) prediction–error distribution and cumulative percentage.

**TABLE 6** | Heat-wise and steel-grade-specific error statistics for the validation heats.

| Case study | RMSE, °C | MAE, °C | Error min, °C | Error max, °C | Type | Type level error metrics | | | |
|---|---|---|---|---|---|---|---|---|---|
| | | | | | | RMSE, °C | MAE, °C | Error min, °C | Error max, °C |
| I | 3.06 | 2.57 | −2.39 | 6.35 | Killed | 2.88 | 2.27 | −5.94 | 8.07 |
| II | 4.28 | 3.57 | −2.27 | 8.07 | | | | | |
| III | 2.52 | 1.92 | −4.47 | 1.61 | | | | | |
| IV | 3.32 | 2.81 | −5.94 | 3.52 | | | | | |
| V | 1.23 | 0.98 | −0.51 | 2.25 | | | | | |
| VI | 2.40 | 2.04 | −3.25 | 3.92 | | | | | |
| VII | 2.47 | 1.90 | −5.06 | 1.56 | | | | | |
| VIII | 2.04 | 1.57 | −3.53 | 0.97 | | | | | |
| IX | 2.38 | 1.87 | −1.74 | 4.52 | | | | | |
| X | 3.01 | 2.74 | −3.61 | 4.72 | | | | | |
| XI | 1.19 | 0.93 | −2.02 | 0.08 | Unkilled | 2.20 | 1.63 | −5.40 | 2.60 |
| XII | 1.57 | 1.30 | −1.99 | 2.60 | | | | | |
| XIII | 4.52 | 4.40 | −5.40 | −3.41 | | | | | |



18693344x, 0, Downloaded from https://onlinelibrary.wiley.com/doi/10.1002/srin.70722 by Daniel Kavi - CochraneAustria , Wiley Online Library on [14/10/2026]. See the Terms and Conditions (https://onlinelibrary.wiley.com/terms-and-conditions) on Wiley Online Library for rules of use; OA articles are governed by the applicable Creative Commons License

a dataset of sufficient size for robust evaluation to assess whether the model reproduces the physical behavior observed in the steel plant process units. The results are summarized in Figure 6a,b.

Figure 6a compares predicted and measured temperatures and shows excellent agreement. In addition, two error bands were evaluated. Overall, 65% of the measurements lie within ±2.5 °C and 91% within ±5 °C of the measured temperature. The agreement is further supported by a root mean squared error (RMSE) of 2.79 °C, a mean absolute error (MAE) of 2.16 °C, and a high coefficient of determination ($R^2$) of 0.98.

Figure 6b shows the error distribution of the difference between measured and predicted temperature, as defined in Equation (4).

$$\text{Error} = T_{\text{predicted}} - T_{\text{measured}} \tag{4}$$

The error distribution is approximately normal and centered near zero, indicating no systematic bias and accurate predictions on average. The cumulative distribution function (CDF) likewise exhibits a normal shape, supporting this conclusion. Only 2.5% of the measurements show an error below −4.9 °C, while the upper bound of the corresponding 2.5% tail is 6.2 °C.

Finally, a detailed error analysis for each investigated heat is provided in Table 6. The killed heats show consistently low deviations, with heat-wise RMSE values between 1.23 and 4.28 °C and MAE values between 0.98 and 3.57 °C. For the unkilled heats, which correspond to the large alloying addition cases, the RMSE ranges from 1.19 to 4.52 °C and the MAE from 0.93 to 4.40 °C.

In addition to the heat-wise error statistics, Table 6 provides summarized error metrics for killed and unkilled steels. These grouped values allow a direct comparison of the model performance for the two investigated steel types. Overall, the results confirm that the hybrid temperature model provides reliable prediction accuracy across the investigated RH treatment cases.

## 5 | Conclusion and Outlook

This study presents a hybrid temperature model for continuous temperature prediction during RH treatment. The main novelty of the work lies in the extension of a previously developed isothermal RH reaction kinetics model with a heat-balance-based temperature module, thereby enabling the consideration of reaction-, alloying-, and process-related thermal effects within a single coupled framework. A mechanistic modeling approach, adopted from an earlier publication [20], is used to describe reaction kinetics, allowing the model to track the chemical heat effects during RH treatment. Thermodynamic data derived from FactSage calculations provide the required mixing, dissolution, and reaction enthalpies, ensuring a physically consistent representation of the heat generated or consumed through chemical reactions and alloying additions. The required thermochemical data are incorporated through precomputed lookup and reaction tables. Thermal losses to the surroundings *via* radiation and convection, together with additional conductive losses during treatment caused by the cooler vacuum vessel, are incorporated using MLR coefficients identified in a previous work [3].

A detailed single-heat analysis of two representative cases shows that the temperature contributions are reproduced accurately over the course of the entire treatment, matching the temperature measurements with a deviation of less than 5 °C. Additional validation across all 13 heats, including 90 samples, demonstrates excellent agreement between predicted and measured temperatures. Overall, 65% of the observations fall within ±2.5 °C and 91% within ±5 °C, with an RMSE of 2.79 °C, an MAE of 2.16 °C, and an $R^2$ of 0.98. The error distribution is approximately normal and centered near zero, indicating no systematic bias, with 2.5% of errors being below −4.9 °C and 2.5% exceeding +6.2 °C.

The presented model forms an additional component of a broader secondary steelmaking model introduced in previous studies [3, 11, 20, 28, 36]. Future work will focus on automated parameter studies and process model optimization using data-driven algorithms such as random search, ant colony optimization, and genetic algorithms. Together, these developments provide a complete secondary steelmaking process model suitable for advanced process control and optimization.

### Author Contributions

**Daniel Kavić:** writing – review & editing, writing – original draft, project administration, methodology, investigation, conceptualization, software, formal analysis. **Michael Bernhard:** writing – review & editing, methodology. **Hannes Prousch:** writing – review & editing. **Roman Rössler:** writing – review & editing, resources. **Christian Bernhard:** supervision, funding acquisition, project administration, writing – review & editing, methodology.


### Acknowledgments

The authors gratefully acknowledge the funding support of K1-MET GmbH, metallurgical competence center. The research program of the K1-MET competence center is supported by COMET (Competence Center for Excellent Technologies), the Austrian program for competence centers. COMET is funded by the Federal Ministry for Innovation, Mobility, and Infrastructure; the Federal Ministry for Economy, Energy, and Tourism; the Federal States of Upper Austria, Tyrol and Styria; the Styrian Business Promotion Agency (SFG); and Standortagentur Tyrol. Furthermore, Upper Austrian Research GmbH continuously supports K1-MET. Besides the public funding from COMET, this research project is partially financed by the Montanuniversitaet Leoben and the industrial partners Primetals Technologies Austria, RHI Magnesita, voestalpine Stahl, and voestalpine Stahl Donawitz.

Open Access funding provided by Montanuniversitat Leoben.


### Conflicts of Interest

The authors declare no conflicts of interest.

### Data Availability Statement

The datasets applied during the current study are based on proprietary industrial process data and cannot be shared due to commercial confidentiality and contractual restrictions.

### References


1. M. Bernhard, P. Presoly, C. Bernhard, S. Hahn, and S. Ilie, "An Assessment of Analytical Liquidus Equations for Fe-C-Si-Mn-Al-P-Alloyed Steels Using DSC/DTA Techniques," *Metallurgical and Materials*





1869344x, 0, Downloaded from https://onlinelibrary.wiley.com/doi/10.1002/srin.70722 by Daniel Kavi - CochraneAustria , Wiley Online Library on [14/10/2026]. See the Terms and Conditions (https://onlinelibrary.wiley.com/terms-and-conditions) on Wiley Online Library for rules of use; OA articles are governed by the applicable Creative Commons License

*Transactions B* 52, no. 5 (2021): 2821–2830, https://doi.org/10.1007/s11663-021-02251-1.

2. P. Presoly, R. Pierer, and C. Bernhard, "Identification of Defect Prone Peritectic Steel Grades by Analyzing High-Temperature Phase Transformations," *Metallurgical and Materials Transactions A* 44, no. 12 (2013): 5377–5388, https://doi.org/10.1007/s11661-013-1671-5.

3. M. Bernhard, D. Kavic, P. Presoly, et al., "A Hybrid Update of the Fe-Si System by DSC, Thermodynamic Modeling and Statistical Learning From Ladle Refining Data of Electrical Steels," *Metallurgical and Materials Transactions B* 56 (2025): 2249–2276, https://doi.org/10.1007/s11663-024-03419-1.

4. P. Deb, A. Mukhopadhyay, A. Ghosh, et al., "Operational Experience With a Mathematical Model for Temperature Prediction in Secondary Steelmaking," *Steel Research* 72, no. 5 (2001): 200–207, https://doi.org/10.1002/srin.200100106.

5. A. Deodhar, U. Singh, R. Shukla, B. P. Gautham, and A. K. Singh, "Fast and Accurate Prediction of Stratified Steel Temperature During Holding Period of Ladle," *Metallurgical and Materials Transactions B* 48, no. 2 (2017): 1217–1229, https://doi.org/10.1007/s11663-016-0874-8.

6. H.-X. Tian and Z.-Z. Mao, "An Ensemble ELM Based on Modified AdaBoost.RT Algorithm for Predicting the Temperature of Molten Steel in Ladle Furnace," *IEEE Transactions on Automation Science and Engineering* 7, no. 1 (2010): 73–80, https://doi.org/10.1109/TASE.2008.2005640.

7. K. Feng, D. He, A. Xu, and H. Wang, "End Temperature Prediction of Molten Steel in LF Based on CBR–BBN," *Steel Research International* 87, no. 1 (2016): 79–86, https://doi.org/10.1002/srin.201400512.

8. I. C. D. Duarte, G. M. de Almeida, and M. Cardoso, "Heat-Loss Cycle Prediction in Steelmaking Plants Through Artificial Neural Network," *Journal of the Operational Research Society* 73, no. 2 (2022): 326–337, https://doi.org/10.1080/01605682.2020.1824552.

9. F. He, D. He, A. Xu, H. Wang, and N. Tian, "Hybrid Model of Molten Steel Temperature Prediction Based on Ladle Heat Status and Artificial Neural Network," *Journal of Iron and Steel Research International* 21, no. 2 (2014): 181–190, https://doi.org/10.1016/S1006-706X(14)60028-5.

10. Z. Xin, J. Zhang, J. Zheng, Y. Jin, and Q. Liu, "A Hybrid Modeling Method Based on Expert Control and Deep Neural Network for Temperature Prediction of Molten Steel in LF," *ISIJ International* 62, no. 3 (2022): 532–541, https://doi.org/10.2355/isijinternational.ISIJINT-2021-251.

11. D. Kavić, M. Bernhard, R. Rössler, L. Schalk, and C. Bernhard, "Enhanced Temperature Prediction in Ladle Furnace Steel Refining: Hybrid Process Modeling Based on Computational Thermodynamics and Statistical Learning Methods," *Metallurgical and Materials Transactions B* 56, no. 5 (2025): 5682–5699, https://doi.org/10.1007/s11663-025-03715-4.

12. K. Feng, H. Wang, A. Xu, and D. He, "Endpoint Temperature Prediction of Molten Steel in RH Using Improved Case-Based Reasoning," *International Journal of Minerals, Metallurgy, and Materials* 20, no. 12 (2013): 1148–1154, https://doi.org/10.1007/s12613-013-0848-7.

13. K. Feng, A. Xu, P. Wu, D. He, and H. Wang, "Case-Based Reasoning Model Based on Attribute Weights Optimized by Genetic Algorithm for Predicting End Temperature of Molten Steel in RH," *Journal of Iron and Steel Research International* 26, no. 6 (2019): 585–592, https://doi.org/10.1007/s42243-019-00264-4.

14. Y. P. Bao, X. Li, and M. Wang, "A Novel Method for Endpoint Temperature Prediction in RH," *Ironmaking Steelmaking* 46, no. 4 (2018): 343–346, https://doi.org/10.1080/03019233.2017.1392104.

15. M. Gu, A. Xu, D. He, H. Wang, and K. Feng, "Prediction Model of End-Point Molten Steel Temperature in RH Refining Based on PCA-CBR," in *11th International Symposium on High-Temperature* (2020), 741–755.

16. J. Yang, J. Zhang, W. Guo, S. Gao, and Q. Liu, "End-Point Temperature Preset of Molten Steel in the Final Refining Unit Based on an Integration of Deep Neural Network and Multi-Process Operation Simulation," *ISIJ International* 61, no. 7 (2021): 2100–2110, https://doi.org/10.2355/isijinternational.ISIJINT-2020-540.

17. C. Baotang, L. Hong, L. Denghui, X. Meng, F. Jia, and W. Zhijie, "Intelligent Prediction for the Temperature of Molten Steel After RH Treatment," *Ironmaking Steelmaking* 51, no. 7 (2024): 638–650, https://doi.org/10.1177/03019233241247397.

18. D. Li, "Membership Clouds and Membership Cloud Generators," *Computer Research and Development* 32, no. 6 (1995): 15–20.

19. K.-P. Zhou, Y. Lin, H.-W. Deng, J. Li, and C. Liu, "Prediction of Rock Burst Classification Using Cloud Model With Entropy Weight," *Transactions of Nonferrous Metals Society of China* 26, no. 7 (2016): 1995–2002, https://doi.org/10.1016/S1003-6326(16)64313-3.

20. D. Kavić, M. Bernhard, R. Rössler, H. Prousch, and C. Bernhard, "Advanced Kinetic Modeling of Ruhrstahl–Heraeus Decarburization: Comprehensive Review and Novel Approach by Coupling Thermodynamics With Tank-in-Series Reactor Concept," *Vacuum*, 254 (2026): 115657, https://doi.org/10.1016/j.vacuum.2026.115657.

21. S. Petersen and K. Hack, "The Thermochemistry Library ChemApp and Its Applications," *International Journal of Materials Research* 98, no. 10 (2007): 935–945, https://doi.org/10.3139/146.101551.

22. C. W. Bale, E. Bélisle, P. Chartrand, et al., "FactSage Thermochemical Software and Databases, 2010-2016," *Calphad* 54 (2016): 35–53, https://doi.org/10.1016/j.calphad.2016.05.002.

23. M. Bernhard and Y.-B. Kang, "A Thermodynamic Model for Si-Deoxidation Equilibria in Liquid Fe and Critical Evaluation of the O Solubility Limit," *ISIJ International* 65, no. 9 (2025): 1279–1288, https://doi.org/10.2355/isijinternational.ISIJINT-2025-113.

24. M.-K. Paek, J.-M. Jang, Y.-B. Kang, J.-J. Pak, and I. Experimental, "Aluminum Deoxidation Equilibria in Liquid Iron: Part," *Metallurgical and Materials Transactions B* 46, no. 4 (2015): 1826–1836, https://doi.org/10.1007/s11663-015-0368-0.

25. M.-K. Paek, J.-J. Pak, and Y.-B. Kang, "Aluminum Deoxidation Equilibria in Liquid Iron: Part II. Thermodynamic Modeling," *Metallurgical and Materials Transactions B* 46, no. 5 (2015): 2224–2233, https://doi.org/10.1007/s11663-015-0369-z.

26. M.-K. Paek, K.-H. Do, Y.-B. Kang, I.-H. Jung, and J.-J. Pak, "Aluminum Deoxidation Equilibria in Liquid Iron: Part III—Experiments and Thermodynamic Modeling of the Fe-Mn-Al-O System," *Metallurgical and Materials Transactions B* 47, no. 5 (2016): 2837–2847, https://doi.org/10.1007/s11663-016-0728-4.

27. A. T. Phan, M.-K. Paek, and Y.-B. Kang, "Phase Equilibria and Thermodynamics of the Fe–Al–C System: Critical Evaluation, Experiment and Thermodynamic Optimization," *Acta Materialia* 79 (2014): 1–15, https://doi.org/10.1016/j.actamat.2014.07.006.

28. D. Kavić, M. Bernhard, R. Rössler, and C. Bernhard, "Simulation of Secondary Metallurgical Processes Using Computational Thermodynamics and Comprehensive Statistical Learning Methods," *Iron & Steel Technology* 12 (2024): 34–46.

29. I. Barin and G. Platzki, *Thermochemical Data of Pure Substances* (VCh Weinheim, 1989).

30. R. G. Berman, T. H. Brown, and H. J. Greenwood, (Atomic Energy of Canada Ltd., 1985).

31. S. K. Saxena, N. Chatterjee, Y. Fei, and G. Shen, *Thermodynamic Data on Oxides and Silicates* (Springer Berlin Heidelberg, 1993).

32. M. W. Chase Jr, "JANAF Thermochemical Tables," *Journal of Physical and Chemical Reference Data* 14 (1985).

33. A. D. Pelton, G. Eriksson, and P. Wu, *Coupled Optimization of Thermodynamic and Phase Diagram Data* (Ecole Polytechnique, 1992).



1869344x, 0, Downloaded from https://onlinelibrary.wiley.com/doi/10.1002/srin.70722 by Daniel Kavi - CochraneAustria , Wiley Online Library on [14/10/2026]. See the Terms and Conditions (https://onlinelibrary.wiley.com/terms-and-conditions) on Wiley Online Library for rules of use; OA articles are governed by the applicable Creative Commons License

34. M. Weinstein and J. F. Elliott, "Solubility of Hydrogen in Liquid Iron Alloys," *Transactions of the Metallurgical Society of AIME* 227, no. 3 (1963): 382–393.

35. G. K. Sigworth and J. F. Elliott, "The Thermodynamics of Liquid Dilute Iron Alloys," *Metal Science* 8 (1974): 298–310, https://doi.org/10.1179/msc.1974.8.1.298.

36. D. Kavić, M. Bernhard, R. Rössler, and C. Bernhard, "Simulation of Secondary Metallurgical Processes by Using Computational Thermodynamics and Comprehensive Statistical Learning Methods," in *AISTech 2024(Proceedings)* (2024), 771–784.



1869344x, 0, Downloaded from https://onlinelibrary.wiley.com/doi/10.1002/srin.70722 by Daniel Kavi - CochraneAustria , Wiley Online Library on [14/10/2026]. See the Terms and Conditions (https://onlinelibrary.wiley.com/terms-and-conditions) on Wiley Online Library for rules of use; OA articles are governed by the applicable Creative Commons License